An analytical shear–lag model for composites with 'brick–and–mortar' architecture considering non-linear matrix response and failure

Soraia Pimenta[a,*], Paul Robinson[b]

[a] The Composites Centre, Department of Mechanical Engineering, South Kensington Campus, Imperial College London, SW7 2AZ, United Kingdom

[b] The Composites Centre, Department of Aeronautics, South Kensington Campus, Imperial College London, SW7 2AZ, United Kingdom

Abstract

Discontinuous composites can combine high stiffness and strength with ductility and damage tolerance. This paper presents an analytical shear–lag model for the tensile response of discontinuous composites with a 'brick–and–mortar' architecture, composed of regularly staggered stiff platelets embedded in a soft matrix. The formulation is applicable to different types of matrix material (e.g. brittle, perfectly–plastic, strain–hardening), which are modelled through generic piecewise–linear and fracture–mechanics consistent shear constitutive laws. Full composite stress–strain curves are calculated in less than 1 second, thanks to an efficient implementation scheme based on the determination of process zone lengths. Parametric studies show that the model bridges the yield–slip (plasticity) theory and fracture mechanics, depending on platelet thickness, platelet aspect–ratio and matrix constitutive law. The potential for using 'brick–and–mortar' architectures to produce composites which are simultaneously strong, stiff and ductile is discussed, and optimised configurations are proposed.

Keywords: 'Brick–and–mortar' architecture, B. Non-linear behaviour, C. Damage mechanics, C. Modelling, C. Stress transfer

1. Introduction

Most natural structural materials combining high stiffness, high strength and damage tolerance (e.g. nacre, bone and spider silk) share a common motif: a discontinuous *'brick–and–mortar'* architecture (see Figure 1a) with staggered stiff inclusions (e.g. fibres or platelets) embedded in a soft matrix [1, 2]. This provides two deformation mechanisms under tension: (i) extension of the inclusions (which dominates in the elastic domain and confers initial stiffness), and (ii) shearing of the matrix (which promotes large deformations and energy dissipation

*Corresponding author.
Email address: soraia.pimenta@imperial.ac.uk (Soraia Pimenta)

Pimenta S, Robinson P (2014). An analytical shear–lag model for composites with 'brick–and–mortar' architecture considering non-linear matrix response and failure. *Composites Science and Technology* 104, 111–124.
DOI:10.1016/j.compscitech.2014.09.001

Nomenclature

Uppercase roman variables	
$\mathcal{A}$	platelet $\mathcal{A}$
$\mathcal{B}$	platelet $\mathcal{B}$
E	tensile stiffness
G	shear stiffness
$\mathcal{G}_c$	critical energy release rate (fracture toughness)
L	characteristic length
N	total number of matrix subdomains
S	shear strength
T	characteristic thickness
V	volume fraction
X	tensile strength

Lowercase roman variables	
l	length
e	tensile failure strain
ℓ	length of matrix subdomain / process zone
n	number of non-central active subdomains
t	thickness
$\mathbf{s}$	subdomains vector
u	displacement
x	location along overlap

Lowercase greek variables	
α	characteristic aspect ratio, $\alpha = L/T$
ε	tensile strain
γ	shear strain
λ	characteristic coefficient, Eq. 5
σ	longitudinal stress
$\Delta\sigma$	difference in platelet stresses, $\Delta\sigma = \sigma^{\mathcal{B}} - \sigma^{\mathcal{A}}$
τ	shear stress

Superscripts	
$\mathtt{b}$	platelet / inclusion ('brick')
$[i]$	matrix subdomain
$\mathtt{m}$	matrix ('mortar')
$\mathtt{pz}$	process zone (matrix damage)
∞	remote
$\star$	ideal geometry for a brittle matrix

Subscripts	
II	mode–II delamination
$\mathtt{M}$	macroscopic response
$\mathtt{uc}$	unit–cell response
$\mathtt{un}$	unloading response

before failure). It is suggested that the combination of these two mechanisms in optimised architectures is key to achieving the impressive performance of many natural composites.

In contrast to natural composites, high-performance Fibre Reinforced Polymers (FRPs) typically use continuous fibres, thus achieving high stiffness and strength but presenting limited ductility. Mimicking the discontinuous architecture of natural composites could potentially overcome this limitation and extend the applicability of FRPs to damage tolerant structures. This requires designing the material microstructure, and thus modelling the effect of discontinuities on the response of composites [3, 4].

One of the most widespread models for discontinuous composites is the Kelly–Tyson yield–slip theory [5]. This assumes that the matrix is perfectly–plastic and transfers stresses between the inclusions by yielding under shear; the performance of the composite is therefore governed by the matrix's shear strength $S^{\mathtt{m}}$. For relatively low aspect–ratio inclusions and neglecting the thickness of the matrix, the strength of the composite X_S^∞ is related to the overlapping inclusion length $l^{\mathtt{b}}$ and inclusion thickness $t^{\mathtt{b}}$ (see Figure 1) by:

$$X_S^\infty = l^{\mathtt{b}} \cdot S^{\mathtt{m}} / t^{\mathtt{b}} \,. \tag{1}$$

This assumes that the inclusions withstand the tensile stresses required to yield the matrix in shear (i.e. the tensile strength of the inclusions is $X^{\mathtt{b}} \geq 2 \cdot X_S^\infty$). The optimal inclusion geometry is therefore defined by a *critical overlapping length* $l^{\mathtt{b}}_{\text{crit}} = X^{\mathtt{b}} \cdot t^{\mathtt{b}} / (2 \cdot S^{\mathtt{m}})$.

An alternative to the *plasticity* or *strength*–based approach in Equation 1 is a *fracture mechanics* or *toughness*–based formulation, which has been applied to discontinuous FRPs with brittle matrices [6, 7]. Assuming that the composite fails when a mode–II crack propagates in the matrix from the ends of the inclusions inwards, and neglecting the effect of friction, the strength of the composite depends on the matrix's (or matrix–inclusion interface's) mode–II fracture toughness $\mathcal{G}_{\mathrm{IIc}}^{\mathtt{m}}$ through:

$$X_{\mathcal{G}}^{\infty} = \sqrt{2 \cdot E^{\mathtt{b}} \cdot \mathcal{G}_{\mathrm{IIc}}^{\mathtt{m}} / t^{\mathtt{b}}}\,. \tag{2}$$

Equations 1 and 2 represent two apparently contradictory criteria whose applicability has been largely debated in the literature [8–13]. It is generally accepted that the former is suitable for ductile matrices (with strain at the ultimate stress above 50%) and the latter for brittle ones (with strain at the ultimate stress below 10%), although the exact ductile–to–brittle transition is yet to be defined. Moreover, Bazant's theory for size effects in quasi–brittle materials [14] suggests that the size of the inhomogeneities relatively to that of the damage process zone also plays a role on the applicability of strength– and toughness–based criteria.

In addition, some details of the matrix's response (e.g. constitutive or geometric strain–hardening) are considered to be fundamental for the outstanding response of some natural composites [3, 4, 15], but are not accounted for in either strength– or toughness–based formulations. Altogether, a more comprehensive modelling framework is required to understand the influence of varying the matrix constitutive law and the geometry of the inclusions, as well as to predict the entire stress–strain curve of discontinuous composites.

The structured architecture of perfectly staggered discontinuous composites allows for the definition of reduced unit–cells, which simplifies their analysis significantly. However, and despite extensive work in modelling composites with 'brick–and–mortar' architecture [3, 4, 15, 16], no formulation in the literature is able to cope with a generic range of inclusion sizes and a generic matrix constitutive law including failure.

This paper presents a model for the influence of discontinuities on the response of composites, depending on the dimensions of the inclusions — hereafter referred to as *platelets* — and matrix shear response. Section 2 develops a new shear–lag analytical model for perfectly staggered discontinuous composites, considering a piecewise linear but otherwise generic matrix constitutive law (including non-linearity and fracture). Section 3 validates analytical results through Finite Elements (FE) analyses, examines local stress fields and the global composite's response, and presents parametric studies on platelet geometry and the matrix's constitutive law. Section 4 discusses the model and its results, its relation with existing literature, and how it can be used to develop improved composites. Finally, Section 5 summarises the main conclusions.

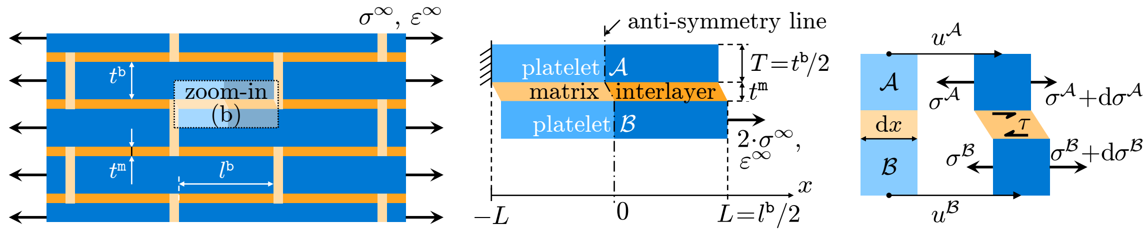

a. Composite with 'brick–and–mortar' architecture.

b. Unit–cell (zoom-in from (a)).

c. Infinitesimal element.

Figure 1: Model overview.

2. Model development

2.1. Shear–lag formulation

Consider the 2D composite with 'brick–and–mortar' architecture represented in Figure 1a, composed of stiff *platelets* (identified by the superscript $\mathtt{b}$) of length $2 \cdot l^{\mathtt{b}}$ and thickness $t^{\mathtt{b}}$, and a soft *matrix* (identified by the superscript $\mathtt{m}$) of thickness $t^{\mathtt{m}}$. The mechanical response of this composite under a remote stress σ^∞ (normalised by the cross–section of platelets only) and strain ε^∞ can be analysed through the unit–cell in Figure 1b. This unit–cell represents the *overlapping region* between two quarter platelets $\mathcal{A}$ and $\mathcal{B}$ separated by a matrix interlayer; it is defined by the *characteristic length* $L = l^{\mathtt{b}}/2$, *characteristic thickness* $T = t^{\mathtt{b}}/2$, and *characteristic aspect–ratio* $\alpha = L/T$.

Assuming a shear–lag model, the platelets support longitudinal stresses $\sigma^{\mathcal{A}}(x)$ and $\sigma^{\mathcal{B}}(x)$, while the matrix transfers shear stresses $\tau(x)$; stresses $\sigma^{\mathcal{A}}(x)$, $\sigma^{\mathcal{B}}(x)$ and $\tau(x)$ are considered uniform in the through–the–thickness direction, which is valid for thin platelets and a thin matrix layer. The equilibrium of an infinitesimal part of the overlapping region (Figure 1c) implies that:

$$\frac{\mathrm{d}\sigma^{\mathcal{B}}(x)}{\mathrm{d}x} = -\frac{\mathrm{d}\sigma^{\mathcal{A}}(x)}{\mathrm{d}x} = \frac{1}{T} \cdot \tau(x) \implies \frac{\mathrm{d}\Delta\sigma(x)}{\mathrm{d}x} = \frac{2}{T} \cdot \tau(x) \,, \quad \text{with} \quad \Delta\sigma(x) \stackrel{\text{def.}}{=} \sigma^{\mathcal{B}}(x) - \sigma^{\mathcal{A}}(x) \,. \tag{3}$$

In addition, the matrix shear deformation $\gamma(x)$ is related to the longitudinal displacement of the platelets $u^{\mathcal{A}}(x)$ and $u^{\mathcal{B}}(x)$. If the platelets are linear–elastic with stiffness $E^{\mathtt{b}}$ (where $E^{\mathtt{b}} = E^{\mathtt{b}}_{11}$ for plane stress and $E^{\mathtt{b}} = E^{\mathtt{b}}_{11}/[1 - (\nu^{\mathtt{b}}_{12})^2]$ for plane strain, being $E^{\mathtt{b}}_{11}$ and $\nu^{\mathtt{b}}_{12}$ respectively the Young's modulus and the major Poisson's ratio of the platelets), then:

$$\gamma(x) = \frac{u^{\mathcal{B}}(x) - u^{\mathcal{A}}(x)}{t^{\mathtt{m}}} \implies \frac{\mathrm{d}\gamma(x)}{\mathrm{d}x} = \frac{\sigma^{\mathcal{B}}(x) - \sigma^{\mathcal{A}}(x)}{t^{\mathtt{m}} \cdot E^{\mathtt{b}}} \implies \frac{\mathrm{d}\gamma(x)}{\mathrm{d}x} = \frac{\Delta\sigma(x)}{t^{\mathtt{m}} \cdot E^{\mathtt{b}}} \,. \tag{4}$$

Defining the shear tangent stiffness of the matrix as $G^{\mathtt{m}}(\gamma) = \mathrm{d}\tau/\mathrm{d}\gamma$, Equations 3 and 4 can be combined in a single differential equation in $\Delta\sigma(x)$:

$$\frac{\mathrm{d}^2\Delta\sigma(x)}{\mathrm{d}x^2} = \frac{G^{\mathtt{m}}(\gamma)}{|G^{\mathtt{m}}(\gamma)|}\cdot\lambda^2\cdot\Delta\sigma(x)\,,\quad \text{where}\quad \lambda \overset{\text{def.}}{=} \sqrt{\frac{2\cdot|G^{\mathtt{m}}(\gamma)|}{T\cdot t^{\mathtt{m}}\cdot E^{\mathtt{b}}}}\,. \tag{5}$$

2.2. Boundary conditions and global response

Following Figure 1b and neglecting longitudinal stress transfer at the ends of the platelets, the boundary conditions at $x = L$ are:

$$\begin{aligned} &\sigma^{\mathcal{A}}(L) = 0 \wedge \sigma^{\mathcal{B}}(L) = 2\cdot\sigma^{\infty} &&\implies && \Delta\sigma_L \overset{\text{def.}}{=} \Delta\sigma(L) = 2\cdot\sigma^{\infty} = \sigma^{\mathcal{A}}(x) + \sigma^{\mathcal{B}}(x)\,;\\ &u^{\mathcal{B}}(L) = 2\cdot L\cdot\varepsilon^{\infty} && \wedge && \gamma_L \overset{\text{def.}}{=} \gamma(L) = [u^{\mathcal{B}}(L) - u^{\mathcal{A}}(L)]/t^{\mathtt{m}}\,. \end{aligned} \tag{6a}$$

Assuming small displacements leads to anti-symmetry at $x = 0$. Consequently,

$$\begin{aligned} &\sigma^{\mathcal{B}}(-x) = \sigma^{\mathcal{A}}(x) &&\implies && \Delta\sigma(0) = 0\,;\\ &\gamma(-x) = \gamma(x) &&\implies && \gamma_0 \overset{\text{def.}}{=} \gamma(0) = \min\left\{\gamma(x),\ x\in[-L,L]\right\}\,. \end{aligned} \tag{6b}$$

From Equation 6a, the global stress–strain curve for the composite is defined as:

$$\sigma^{\infty} = \frac{\Delta\sigma_L}{2} \qquad \text{and} \qquad \varepsilon^{\infty} = \frac{\Delta\sigma_L}{2\cdot E^{\mathtt{b}}} + \frac{t^{\mathtt{m}}\cdot\gamma_L}{2\cdot L}\,, \tag{7a}$$

where the strain was calculated as $\varepsilon^{\infty} = [u^{\mathcal{A}}(L) + \gamma_L\cdot t^{\mathtt{m}}]/[2\cdot L]$, with:

$$u^{\mathcal{A}}(L) = \int_{x=-L}^{L}\frac{\sigma^{\mathcal{A}}(x)}{E^{\mathtt{b}}}\,\mathrm{d}x = \int_{x=0}^{L}\frac{\sigma^{\mathcal{A}}(x)+\sigma^{\mathcal{B}}(x)}{E^{\mathtt{b}}}\,\mathrm{d}x = \frac{L\cdot\Delta\sigma_L}{E^{\mathtt{b}}}\,. \tag{7b}$$

2.3. Matrix response and local solutions

Consider that the matrix has a generic piecewise linear constitutive law in shear, as exemplified in Figure 2a. Each linear piece or *subdomain* (identified by the index $i = \{1,\cdots,N{+}1\}$, for a matrix with N load–bearing subdomains) is defined within $\gamma\in[\gamma^{[i-1]},\gamma^{[i]}]$, and characterised by the tangent stiffness $G^{[i]} \overset{\text{def.}}{=} G^{\mathtt{m}}(\gamma) = (\tau^{[i]} - \tau^{[i-1]})/(\gamma^{[i]} - \gamma^{[i-1]})$. The first subdomain is linear elastic, and the shear modulus of the matrix is $G^{\mathtt{m}}_{\mathrm{el}} \overset{\text{def.}}{=} G^{[1]}$. The final subdomain and the shear strain at the formation of a crack tip ($\gamma^{[N]}$) can be adjusted to ensure a correct energy dissipation; assuming that the mode–II critical energy release rate of the matrix ($\mathcal{G}^{\mathtt{m}}_{\mathrm{IIc}}$, hereby designated as fracture toughness) is independent of the modelled matrix thickness and that $\gamma^{[N]} > \gamma^{[N-1]}$, then:

$$\mathcal{G}^{\mathtt{m}}_{\mathrm{IIc}} = t^{\mathtt{m}}\cdot\int_{\gamma=0}^{\gamma^{[N]}}\tau(\gamma)\,\mathrm{d}\gamma \implies \gamma^{[N]} = \gamma^{[N-1]} + \frac{2}{\tau^{[N-1]}}\cdot\left[\frac{\mathcal{G}^{\mathtt{m}}_{\mathrm{IIc}}}{t^{\mathtt{m}}} - \sum_{i=1}^{N-1}\frac{\tau^{[i]}+\tau^{[i-1]}}{2}\cdot\left(\gamma^{[i]}-\gamma^{[i-1]}\right)\right]. \tag{8}$$

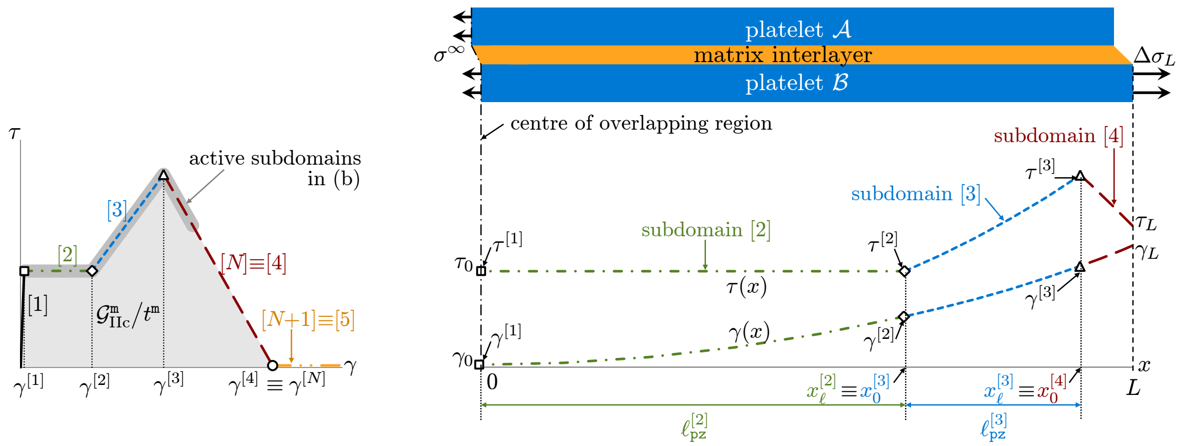

a. Constitutive law of the matrix with $N = 4$ subdomains.

b. Half overlapping region ($x \in [0, L]$) with active subdomains $\mathbf{s} = \{2, 3, 4\}$. Subdomain $[i=2]$ is active in $x \in [0, x^{[2]}_\ell]$, with $\gamma_0 \geq \gamma^{[1]}$ and $\gamma(x^{[2]}_\ell) = \gamma^{[2]}$. Subdomain $[i+1=3]$ is active in $x \in [x^{[3]}_0, x^{[3]}_\ell]$, with $x^{[3]}_0 \equiv x^{[2]}_\ell$ and $\gamma(x^{[3]}_\ell) = \gamma^{[3]}$. Subdomain $[i+2=4]$ is active in $x \in [x^{[4]}_0, L]$, with $x^{[4]}_0 \equiv x^{[3]}_\ell$ and $\gamma_L \leq \gamma^{[4]}$.

Figure 2: Definition of matrix subdomains in the unit–cell of composites with 'brick–and–mortar' architecture.

Table 1: Local solution for response of an overlap in the subdomain $[i]$, active within $x \in [\bar{x}_0, \bar{x}_\ell]$.

Differential equation ($\bar{G} \equiv G^{[i]}$ and $\bar{\lambda} \equiv \lambda^{[i]}$)		Local stress and strain fields under the following boundary conditions: $\gamma(\bar{x}_0) = \bar{\gamma}_0$, $\tau(\bar{x}_0) = \bar{\tau}_0 = \tau(\bar{\gamma}_0)$ and $\Delta\sigma(\bar{x}_0) = \Delta\bar{\sigma}_0$	
Positive stiffness, $\bar{G} > 0$: $\frac{\mathrm{d}^2}{\mathrm{d}x^2}\Delta\sigma(x) = \bar{\lambda}^2 \Delta\sigma(x)$	(a)	$\begin{cases} \Delta\sigma(x) = \Delta\bar{\sigma}_0 \cdot \cosh\left[\bar{\lambda}\cdot(x-\bar{x}_0)\right] + \dfrac{2}{\bar{\lambda}\cdot T}\cdot\bar{\tau}_0\cdot\sinh\left[\bar{\lambda}\cdot(x-\bar{x}_0)\right] \\ \tau(x) = \bar{\tau}_0\cdot\cosh\left[\bar{\lambda}\cdot(x-\bar{x}_0)\right] + \dfrac{\bar{\lambda}\cdot T}{2}\cdot\Delta\bar{\sigma}_0\cdot\sinh\left[\bar{\lambda}\cdot(x-\bar{x}_0)\right] \\ \gamma(x) = \bar{\gamma}_0 + \dfrac{\bar{\tau}_0}{\lvert\bar{G}\rvert}\cdot\left(\cosh\left[\bar{\lambda}\cdot(x-\bar{x}_0)\right]-1\right) + \dfrac{\Delta\bar{\sigma}_0}{\bar{\lambda}\cdot t^{\mathrm{m}}\cdot E^{\mathrm{b}}}\cdot\sinh\left[\bar{\lambda}\cdot(x-\bar{x}_0)\right] \end{cases}$	(b)
Zero stiffness, $\bar{G} = 0$: $\frac{\mathrm{d}^2}{\mathrm{d}x^2}\Delta\sigma(x) = 0$	(c)	$\begin{cases} \Delta\sigma(x) = \Delta\bar{\sigma}_0 + \dfrac{2}{T}\cdot\bar{\tau}_0\cdot(x-\bar{x}_0) \\ \tau(x) = \bar{\tau}_0 \\ \gamma(x) = \bar{\gamma}_0 + \dfrac{\bar{\tau}_0}{T\cdot t^{\mathrm{m}}\cdot E^{\mathrm{b}}}\cdot(x-\bar{x}_0)^2 + \dfrac{\Delta\bar{\sigma}_0}{t^{\mathrm{m}}\cdot E^{\mathrm{b}}}\cdot(x-\bar{x}_0) \end{cases}$	(d)
Negative stiffness, $\bar{G} < 0$: $\frac{\mathrm{d}^2}{\mathrm{d}x^2}\Delta\sigma(x) = -\bar{\lambda}^2 \Delta\sigma(x)$	(e)	$\begin{cases} \Delta\sigma(x) = \Delta\bar{\sigma}_0 \cdot \cos\left[\bar{\lambda}\cdot(x-\bar{x}_0)\right] + \dfrac{2}{\bar{\lambda}\cdot T}\cdot\bar{\tau}_0\cdot\sin\left[\bar{\lambda}\cdot(x-\bar{x}_0)\right] \\ \tau(x) = \bar{\tau}_0\cdot\cos\left[\bar{\lambda}\cdot(x-\bar{x}_0)\right] - \dfrac{\bar{\lambda}\cdot T}{2}\cdot\Delta\bar{\sigma}_0\cdot\sin\left[\bar{\lambda}\cdot(x-\bar{x}_0)\right] \\ \gamma(x) = \bar{\gamma}_0 + \dfrac{\bar{\tau}_0}{\lvert\bar{G}\rvert}\cdot\left(1-\cos\left[\bar{\lambda}\cdot(x-\bar{x}_0)\right]\right) + \dfrac{\Delta\bar{\sigma}_0}{\bar{\lambda}\cdot t^{\mathrm{m}}\cdot E^{\mathrm{b}}}\cdot\sin\left[\bar{\lambda}\cdot(x-\bar{x}_0)\right] \end{cases}$	(f)
Fully debonded, $\bar{G} = 0 \wedge \tau = 0$: $\frac{\mathrm{d}^2}{\mathrm{d}x^2}\Delta\sigma(x) = 0$	(g)	$\begin{cases} \Delta\sigma(x) = \sigma^\infty \\ \tau(x) = 0 \\ \gamma(x) = \gamma^{[N]} + \dfrac{\sigma^\infty}{t^{\mathrm{m}}\cdot E^{\mathrm{b}}}\cdot(x-\bar{x}_0) \end{cases}$	(h)

In a generic constitutive law, four types of matrix subdomain may be considered: linear–elastic / strain–hardening ($G^{[i]} > 0$), perfectly–plastic ($G^{[i]} = 0 \wedge \tau > 0$), strain–softening ($G^{[i]} < 0$), and fully–fractured or debonded ($G^{[i]} = 0 \wedge \tau = 0$). Depending on the loading state, a subdomain may be *active* in the overlapping region within $x \in [x_0^{[i]}, x_\ell^{[i]}]$ (Figure 2b). Table 1 shows the solution $\Delta\sigma(x)$ of the governing differential equation (Eq. 5) for each type of subdomain. Stress and strain fields in platelets and matrix are subsequently defined as:

$$\tau(x) = \frac{T}{2} \cdot \frac{\mathrm{d}}{\mathrm{d}x} \Delta\sigma(x)\,; \tag{9a}$$

$$\gamma(x) = \gamma_0 + \frac{1}{t^{\mathrm{m}} \cdot E^{\mathrm{b}}} \cdot \int_{z=0}^{x} \Delta\sigma(z)\,\mathrm{d}z\,; \tag{9b}$$

$$\sigma^{\mathcal{A}}(x) = \frac{\Delta\sigma_L - \Delta\sigma(x)}{2}\,; \tag{9c}$$

$$\sigma^{\mathcal{B}}(x) = \frac{\Delta\sigma_L + \Delta\sigma(x)}{2}\,. \tag{9d}$$

2.4. Length of process zones

The stress and strain fields presented in Table 1 can be used to determine the Length of the Process Zone (LPZ) required to develop the matrix's strain interval $\gamma \in [\bar{\gamma}_0, \bar{\gamma}_\ell]$ in a segment of the overlapping region ($x \in [\bar{x}_0, \bar{x}_\ell]$, with $\bar{x}_0 < \bar{x}_\ell$). This is formally defined as:

$$\ell = \ell\big[\bar{\gamma}_0 \equiv \gamma(\bar{x}_0),\ \bar{\gamma}_\ell \equiv \gamma(\bar{x}_\ell),\ \Delta\bar{\sigma}_0 \equiv \Delta\sigma(\bar{x}_0)\big] \stackrel{\text{def.}}{=} \bar{x}_\ell - \bar{x}_0\,. \tag{10a}$$

This concept can be applied to calculate the LPZ associated with developing completely a single subdomain $[i]$ from $x=0$ to $x=x_\ell^{[i]}$ (see for instance $i = 2$ in Figure 2b), defined as:

$$\ell_{\mathtt{pz}}^{[i]} = \ell\big[\bar{\gamma}_0 \equiv \gamma^{[i-1]},\ \bar{\gamma}_\ell \equiv \gamma^{[i]},\ \Delta\bar{\sigma}_0 \equiv \Delta\sigma(0) = 0\big] \stackrel{\text{def.}}{=} x_\ell^{[i]}\,. \tag{10b}$$

Expressions for LPZs are shown in Table 2. This definition can be further extended to any set of consecutive subdomains $[i, \ldots, i{+}n]$ in the overlapping region (e.g. $i = \{2, 3, 4\}$ in Figure 2b). In that case, the multiple LPZ of the $n{+}1$ subdomains can be calculated recursively as:

$$\ell_{\mathtt{pz}}^{[i,i+1,\ldots,i+n-1,i+n]} \stackrel{\text{def.}}{=} \ell_{\mathtt{pz}}^{[i,i+1,\ldots,i+n-1]} + \ell\left[\bar{\gamma}_0 = \gamma^{[i+n-1]}, \bar{\gamma}_\ell = \gamma^{[i+n]}, \Delta\bar{\sigma}_0 = \Delta\sigma_\ell^{[i+n-1]}\right]\,, \tag{10c}$$

where $\Delta\sigma_\ell^{[j]}$ is calculated in Table 3 for $j \in [i{+}1, i{+}n{-}1]$, and $\Delta\sigma_\ell^{[i-1]} = \Delta\sigma_0 = 0$.

For a matrix constitutive law with N load–bearing subdomains, all relevant LPZs (omitting the infinite LPZs $\ell_{\mathtt{pz}}^{[1,\ldots]}$ and $\ell_{\mathtt{pz}}^{[\ldots,N+1]}$) can be organised in a *process zone matrix*:

$$\mathbf{L}_{\mathtt{pz}} \stackrel{\text{def.}}{=} \begin{bmatrix} \ell_{\mathtt{pz}}^{[2]} & \ell_{\mathtt{pz}}^{[2,3]} & \cdots & \ell_{\mathtt{pz}}^{[2,3,\ldots,N-1]} & \ell_{\mathtt{pz}}^{[2,3,\ldots,N-1,N]} \\ \ell_{\mathtt{pz}}^{[3]} & \ell_{\mathtt{pz}}^{[3,4]} & \cdots & \ell_{\mathtt{pz}}^{[3,4,\ldots,N]} & \\ \vdots & \vdots & \iddots & & \\ \ell_{\mathtt{pz}}^{[N-1]} & \ell_{\mathtt{pz}}^{[N-1,N]} & & & \\ \ell_{\mathtt{pz}}^{[N]} & & & & \end{bmatrix}\,. \tag{11}$$

Table 2: Length of process zones.

Type of subdomain	Length for developing the matrix strain interval $\gamma \in [\bar\gamma_0, \bar\gamma_\ell]$	Length of process zone for subdomain $[i]$ (for $\Delta\bar\sigma_0^{[i]} \equiv 0$, $\bar\gamma_0 \equiv \gamma^{[i-1]}$, $\bar\gamma_\ell \equiv \gamma^{[i]}$)
Positive stiffness	$\ell = \frac{2}{\bar\lambda}\cdot\text{atanh}\left[\frac{\bar\lambda\cdot T}{2\cdot(\bar\tau_0+\bar\tau_\ell)}\cdot \cdot\left(\sqrt{\Delta\bar\sigma_0{}^2 + \left(\frac{2}{\bar\lambda\cdot T}\right)^2\cdot(\bar\tau_\ell^2-\bar\tau_0^2)} - \Delta\bar\sigma_0\right)\right]$ (a)	$\ell_{\texttt{pz}}^{[i]} = \frac{2}{\lambda^{[i]}}\cdot\text{atanh}\left[\sqrt{\frac{\tau^{[i]}-\tau^{[i-1]}}{\tau^{[i]}+\tau^{[i-1]}}}\right]$ (b) Linear–elastic subdomain, $i=1$, $\tau^{[0]}=0$: $\ell_{\texttt{pz}}^{[1]} = \frac{2}{\lambda^{[1]}}\cdot\text{atanh}(1) = \infty$ (c)
Zero stiffness	$\ell = \frac{T}{2\cdot\bar\tau_0}\cdot\left(\sqrt{\Delta\bar\sigma_0{}^2 + \frac{4\cdot t^{\texttt{m}}\cdot E^{\texttt{b}}}{T}\cdot\bar\tau_0\cdot(\bar\gamma_\ell-\bar\gamma_0)} - \Delta\bar\sigma_0\right)$ (d)	$\ell_{\texttt{pz}}^{[i]} = \sqrt{T\cdot t^{\texttt{m}}\cdot E^{\texttt{b}}\cdot\frac{\gamma^{[i]}-\gamma^{[i-1]}}{\tau^{[i]}}}$ (e)
Negative stiffness	$\ell = \frac{2}{\bar\lambda}\cdot\text{atan}\left[\frac{\bar\lambda\cdot T}{2\cdot(\bar\tau_0+\bar\tau_\ell)}\cdot \cdot\left(\sqrt{\Delta\bar\sigma_0{}^2 + \left(\frac{2}{\bar\lambda\cdot T}\right)^2\cdot(\bar\tau_0^2-\bar\tau_\ell^2)} - \Delta\bar\sigma_0\right)\right]$ (f)	$\ell_{\texttt{pz}}^{[i]} = \frac{2}{\lambda^{[i]}}\cdot\text{atan}\left[\sqrt{\frac{\tau^{[i-1]}-\tau^{[i]}}{\tau^{[i-1]}+\tau^{[i]}}}\right]$ (g) Decohesion subdomain, $i=N$, $\tau^{[N]}=0$: $\ell_{\texttt{pz}}^{[N]} = \frac{2}{\lambda^{[N]}}\cdot\text{atan}(1) = \frac{\pi}{2\cdot\lambda^{[N]}}$ (h)
Fully debonded ($i=N+1$)	$\ell = \frac{t^{\texttt{m}}\cdot E^{\texttt{b}}}{\sigma^\infty}\cdot(\bar\gamma_\ell-\gamma^{[N]})$, as $G^{[N+1]}=\tau^{[N]}=\tau^{[N+1]}=0$ (i)	$\ell_{\texttt{pz}}^{[N+1]} = \infty$ (j)

Table 3: Longitudinal stress difference $\Delta\sigma_\ell^{[j]}$ at the transition $x_\ell^{[j]} \equiv x_0^{[j+1]}$ between subdomains $[j]$ and $[j+1]$. Subdomain $[j]$ is defined within $[x_0^{[j]}, x_\ell^{[j]}]$, with $\Delta\sigma(x_0^{[j]}) \equiv \Delta\sigma_0^{[j]}$, $\gamma(x_0^{[j]}) \equiv \gamma_0^{[j]}$, and $\gamma(x_\ell^{[j]}) \equiv \gamma^{[j]}$.

Subdomain $[j]$	Stress difference at $x_\ell^{[j]}$, where $\tau_0^{[j]} = \tau(\gamma_0^{[j]})$ and $\begin{cases}\Delta\sigma_0^{[j]} = 0 \quad\quad \wedge\, \gamma_0^{[j]} = \gamma_0 \quad, j=i \\ \Delta\sigma_0^{[j]} = \Delta\sigma_\ell^{[j-1]} \wedge \gamma_0^{[j]} = \gamma^{[j-1]}, j \geq i+1\end{cases}$
Positive stiffness	$\Delta\sigma_\ell^{[j]} = \sqrt{\left(\Delta\sigma_0^{[j]}\right)^2 + \left(\frac{2}{\lambda^{[j]}\cdot T}\right)^2\cdot\left[(\tau^{[j]})^2 - (\tau_0^{[j]})^2\right]}$ (a)
Zero stiffness	$\Delta\sigma_\ell^{[j]} = \sqrt{\left(\Delta\sigma_0^{[j]}\right)^2 + \frac{4\cdot t^{\texttt{m}}\cdot E^{\texttt{b}}}{T}\cdot\tau^{[j]}\cdot\left[\gamma^{[j]} - \gamma_0^{[j]}\right]}$ (b)
Negative stiffness	$\Delta\sigma_\ell^{[j]} = \sqrt{\left(\Delta\sigma_0^{[j]}\right)^2 + \left(\frac{2}{\lambda^{[j]}\cdot T}\right)^2\cdot\left[(\tau_0^{[j]})^2 - (\tau^{[j]})^2\right]}$ (c)

2.5. Evolution of subdomains during progressive loading

Consider the overlapping region represented in Figure 2, in which the matrix has $N \equiv 4$ load–bearing subdomains. For the value of γ_0 considered, the range of $n{+}1$ *active subdomains* can be described by a *subdomains vector* $\mathbf{s} = \{i, i{+}1, \ldots, i{+}n{-}1, i{+}n\} \equiv \{2, 3, 4\}$. The full equilibrium response of the unit–cell can be tracked by monotonically increasing γ_0 from zero (undeformed state, $\mathbf{s} = \{1\}$) to $\gamma^{[N]}$ (fully–delaminated, $\mathbf{s} = \{N{+}1\} \equiv \{5\}$).

The evolution of $\mathbf{s}$ with γ_0 depends on the relation between the matrix's LPZs and the characteristic length L. Take for instance the subdomains vector at the instant k represented in Figure 2, $\mathbf{s}_k = \{2, 3, 4\}$; the next subdomains vector will be $\mathbf{s}_{k+1} = \{3, 4\}$ if $\ell_{\mathtt{pz}}^{[3,4]} > L$ (in which case γ_0 reaches $\gamma^{[2]}$ before γ_L reaches $\gamma^{[4]}$), or $\mathbf{s}_{k+1} = \{2, 3, 4, 5\}$ if $\ell_{\mathtt{pz}}^{[3,4]} < L$ (in which case γ_L reaches $\gamma^{[4]}$ before γ_0 reaches $\gamma^{[2]}$). Figure 3 presents all possible cases for the evolution of active subdomains in a unit–cell with $N = 4$.

In order to generalise the algorithm in Figure 3 for any N, note that the generic configuration $\mathbf{s}_k = \{i, i{+}1, \ldots, i{+}n\}$ of active subdomains may change by one of the two events:

- *Deactivation* of subdomain $[i]$ at $x = 0$, when $\gamma_0 = \gamma^{[i]}$, if $\ell_{\mathtt{pz}}^{[i+1,\ldots,i+n]} > L$ and $n > 0$. The new subdomains vector is thus $\mathbf{s}_{k+1} = \{i{+}1\,, \ldots\,, i{+}n\}$;
- *Activation* of subdomain $[i{+}n{+}1]$ at $x = L$, when $\gamma_L = \gamma^{[i+n]}$, if $\ell_{\mathtt{pz}}^{[i+1,\ldots,i+n]} < L$ or $n = 0$. The new subdomains vector is thus $\mathbf{s}_{k+1} = \{i\,, i{+}1\,, \ldots\,, i{+}n\,, i{+}n{+}1\}$.

These two events cannot occur simultaneously (unless $\ell_{\mathtt{pz}}^{[i+1,\ldots,i+n]} = L$ is exactly verified). The only exception is when $\mathbf{s}_k = \{N\}$, which is directly followed by $\mathbf{s}_{k+1} = \{N{+}1\}$; in this case, the entire overlapping region cracks (i.e. reaches $\gamma(x) = \gamma^{[N]} \wedge \tau(x) = 0$) at once; this can be seen by imposing $\bar{x}_0 = 0$, $\Delta\bar{\sigma}_0 = \Delta\sigma_0 = 0$ and $\bar{\tau}(L) = \tau_L = 0$ in Table 1, Eq.(f).

The process zone matrix $\mathbf{L}_{\mathtt{pz}}$ (Equation 11) is therefore sufficient to establish the entire sequence of active subdomains, from $\mathbf{s} = \{1\}$ (when $\gamma_0 = 0$) to $\mathbf{s} = \{N{+}1\}$ (when $\gamma_0 = \gamma^{[N]}$). The transition between subdomain vectors $\mathbf{s}_k$ and $\mathbf{s}_{k+1}$ is defined by the *transition strain* $\gamma_0 \equiv \gamma_k^{\mathrm{crit}} \in [0, \gamma^{[N]}]$, as derived in Table 4.

2.6. Model implementation

Figure 4 proposes a numerical implementation of the proposed model. Once all required functions are defined according to the derivations above, stress and strain fields can be calculated without any iterative process. The full equilibrium response of a composite with ‘brick–and–mortar’ architecture and non-linear matrix is thus calculated in less than 1 second.

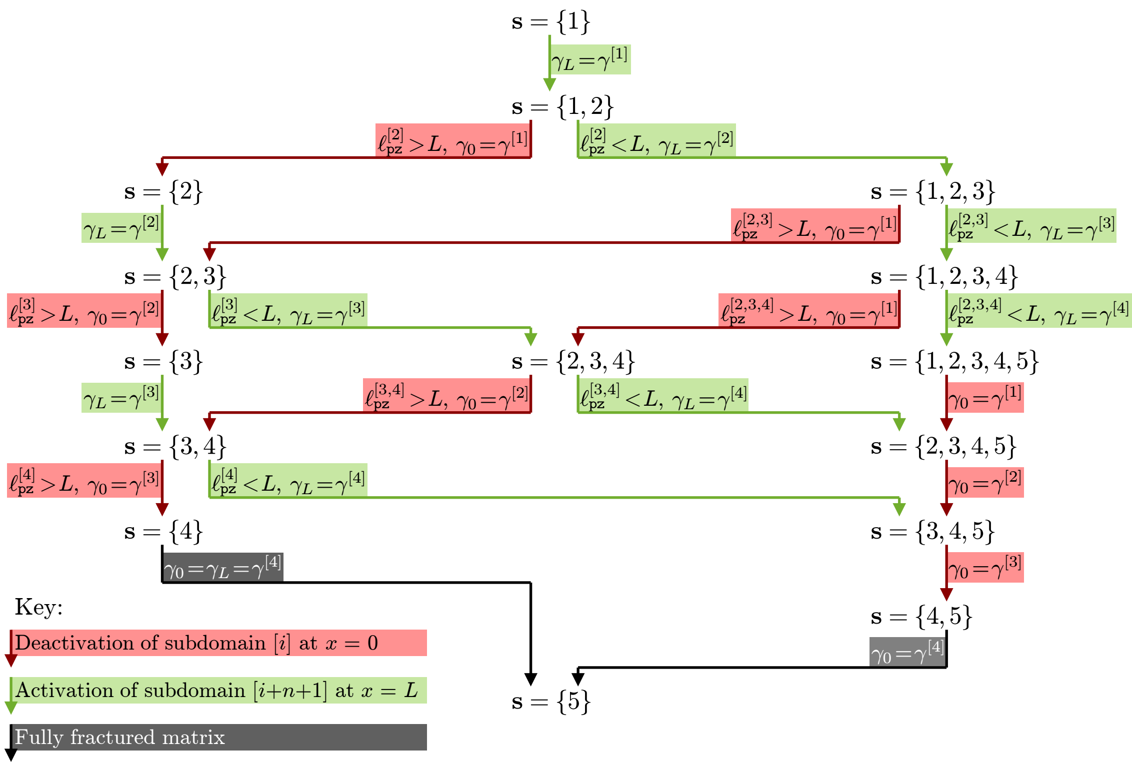

Figure 3: Evolution of active subdomains during progressive loading of a composite with 'brick–and–mortar' architecture, considering a matrix constitutive law with 4 subdomains (followed by fracture, represented as $i=N+1=5$).

Table 4: Transition shear strain γ_k^{crit} (defined at the centre of the overlapping region, $\gamma_k^{\text{crit}}\equiv\gamma_0$) between configurations $\mathbf{s}_k=\{i,\cdots,i+n\}$ and $\mathbf{s}_{k+1}$.

Type of transition			Transition strain	
Deactivation:	$n>0\wedge\ell_{\text{pz}}^{[i+1,\ldots,i+n]}>L$, $\mathbf{s}_{k+1}=\{i+1,\cdots,i+n\}$		$\gamma_0=\gamma^{[i]}\implies\gamma_k^{\text{crit}}=\gamma^{[i]}$	(a)
Activation:	$n=0$, $\mathbf{s}_{k+1}=\{i,i+1\}$	Positive stiffness:	$\gamma_L=\gamma^{[i]}\implies\gamma_k^{\text{crit}}=\gamma^{[i]}-\dfrac{\tau^{[i]}}{\lvert G^{[i]}\rvert}\cdot\left(1-\dfrac{1}{\cosh\left[\lambda^{[i]}\cdot L\right]}\right)$	(b)
		Zero stiffness:	$\gamma_L=\gamma^{[i]}\implies\gamma_k^{\text{crit}}=\gamma^{[i]}-\tau^{[i]}\cdot\dfrac{L^2}{T\cdot t^{\mathtt{m}}\cdot E^{\mathtt{b}}}$	(c)
		Negative stiffness:	$\gamma_L=\gamma^{[i]}\implies\gamma_k^{\text{crit}}=\gamma^{[i]}-\dfrac{\tau^{[i]}}{\lvert G^{[i]}\rvert}\cdot\left(\dfrac{1}{\cos\left[\lambda^{[i]}\cdot L\right]}-1\right)$	(d)
Activation:	$n>0\wedge\ell_{\text{pz}}^{[i]}>L$, $\mathbf{s}_{k+1}=\{i,\cdots,i+n+1\}$		$\gamma_L=\gamma^{[i+n]}\implies\gamma_k^{\text{crit}}\in\left[\gamma_{k-1}^{\text{crit}},\gamma^{[i]}\right]:$ $\ell\left[\bar{\gamma}_0\equiv\gamma_k^{\text{crit}},\ :\bar{\gamma}_\ell\equiv\gamma^{[i+n]},\ \Delta\bar{\sigma}_0\equiv0\right]=L$	(e)

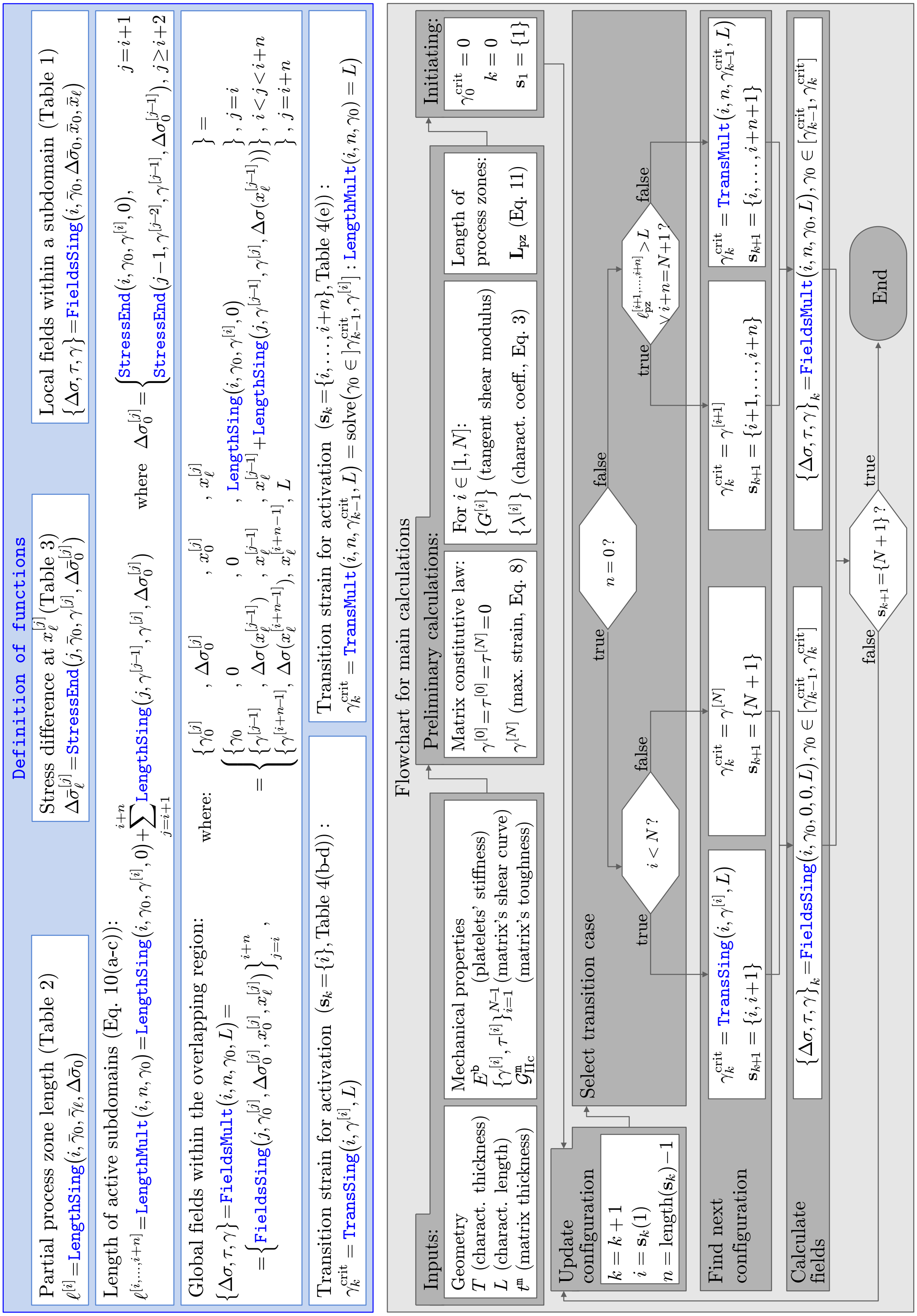

Figure 4: Implementation of the proposed model for the response of composites with 'brick–and–mortar' architecture.

3. Results

3.1. Analysis of model predictions

Figure 5 shows the outputs of the analytical model for the nominal inputs shown in Table 5, and assuming the strain–hardening matrix response defined in Figure 5a. The stress–strain curves predicted for composites with two platelet geometries — thick ($L = 1$ mm, $\alpha = 10$) and slender ($L = 5$ mm, $\alpha = 50$) — are shown in Figure 5b; results are validated against FE simulations of the unit–cell in Figure 1b (described in Appendix A).

Figures 5c–5d show the evolution of stress fields in the thick configuration ($L = 1$ mm). Matrix yielding initiates at the ends of the platelets (point ① in Figure 5b), but quickly extends to the entire overlapping length (the plastic plateau is fully developed before point ②). Further loading leads to the initiation and progress of matrix strain–hardening (point ③), and to the onset of strain–softening at the platelets' ends (when $\tau(\pm L) \equiv S^{\mathtt{m}}$). The softened region extends inwards and the applied stress reach its peak (point ④), after which the material progressively unloads (point ⑤). Due to the low aspect–ratio platelets, matrix shear stresses are relatively homogeneous, and platelet stresses have a quasi–linear profile (except for the elastic domain, point ①). The overall stress–strain curve (Figure 5b, $L = 1$ mm) is very non-linear, and resembles that of the matrix (Figure 5a, strain–hardening curve).

Figures 5e–5f show the evolution of stress fields in the slender configuration ($L = 5$ mm). The matrix starts yielding very early (before point ① in Figure 5b), and further loading develops plastic and strain–hardening subdomains at the platelets' ends (point ②). This is followed by matrix softening and formation of two mode–II crack tips ($\tau(\pm L) = 0$, point ③), which propagate inwards at constant load until the damage process zones meet at the centre of the overlapping region (point ④). Consequently, the matrix progressively loses its load–transfer ability and the platelets unload, creating an instability under displacement control (illustrated by point ⑤). Due to the slender geometry, shear stresses are transferred only at the ends of the overlapping region during most of the loading phase (points ① to ③), and the overall stress–strain curve is quasi-linear up to crack–tip formation.

3.2. Effect of the matrix constitutive law and platelet aspect–ratio

Figure 6 shows the response of composites with different characteristic aspect–ratio (α) and various shapes of the matrix constitute law (see Figure 5a). The overall stress–strain

Table 5: Nominal dimensions and properties for shear overlap models.

Geometry		platelet properties		Matrix properties		
T (mm)	$t^{\mathtt{m}}$ (mm)	$E^{\mathtt{b}}$ (GPa)	$X^{\mathtt{b}}$ (MPa)	$G^{\mathtt{m}}_{\mathrm{el}}$ (GPa)	$S^{\mathtt{m}}$ (MPa)	$\mathcal{G}^{\mathtt{m}}_{\mathrm{IIc}}$ (kJ/m^2)
0.100	0.010	100	2500	1.0	50	1.0

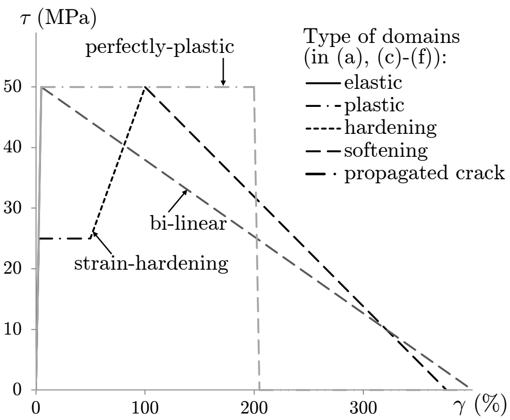

a. Matrix shear responses considered in this study, with coordinates (γ[%], τ[MPa]) as follows:
strain–hard.: (2.5,25); (50,25); (100,50); (376,0);
bi-linear: (5,50); (400,0);
perfectly–plastic: (5,50); (200,50); (205,0).

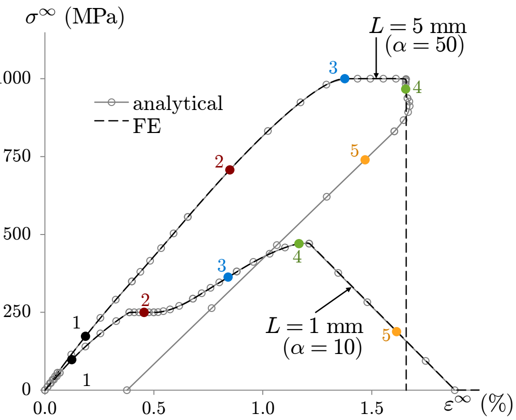

b. Global stress–strain response of composites with a strain–hardening matrix, as predicted by the analytical and plane–stress FE models.

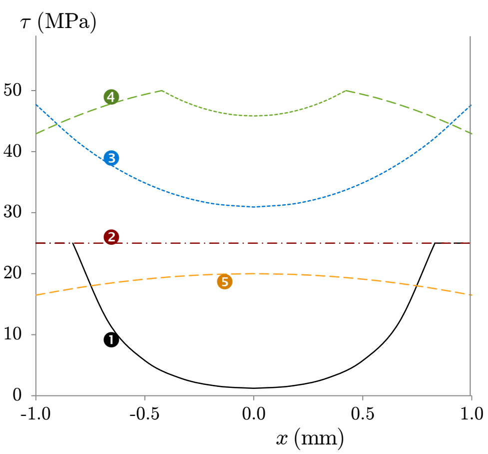

c. Shear stresses the strain–hardening matrix, for $L = 1$ mm ($\alpha = 10$).

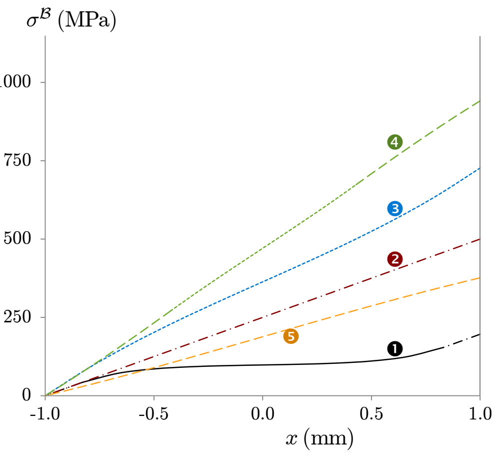

d. Platelet stresses for $L = 1$ mm ($\alpha = 10$) and a strain–hardening matrix.

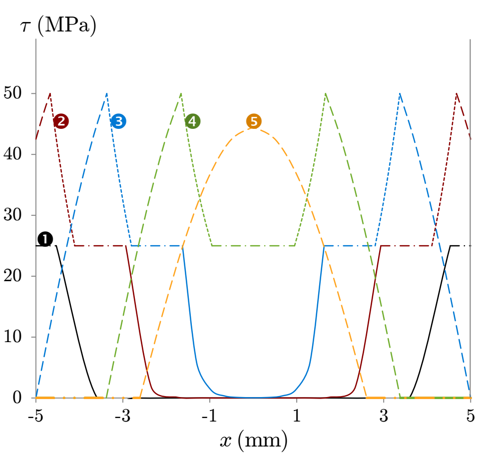

e. Shear stresses for the strain–hardening matrix, for $L = 5$ mm ($\alpha = 50$).

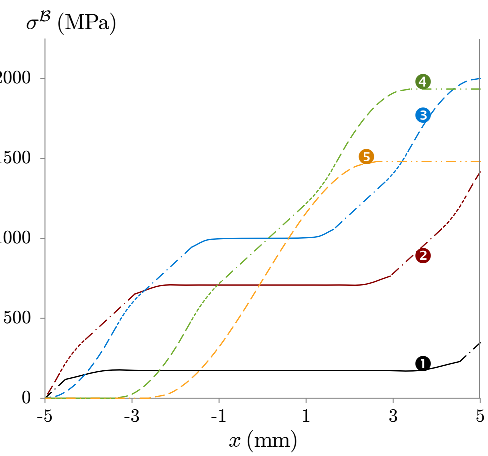

f. Platelet stresses for $L = 5$ mm ($\alpha = 50$) and a strain–hardening matrix.

Figure 5: Response of composites with 'brick–and–mortar' architecture, assuming the nominal inputs shown in Table 5.

curve of low aspect–ratio configurations resembles the matrix constitutive law (e.g. compare the curves for $\alpha = 5$ in Figures 6a–6c with those in Figure 5a); however, as the characteristic aspect–ratio increases, the composite's response becomes quasi-linear and almost independent of the matrix type (e.g. curves for $\alpha = 100$ in Figures 6a–6c).

For relatively thick configurations ($\alpha \lesssim 10$), the strength of the composite increases with the characteristic aspect–ratio, in agreement with a yield criterion (Equation 1, see Figure 6d). For slender configurations ($\alpha \gtrsim 30$), on the contrary, the model predicts that the composite's strength becomes independent of aspect ratio and converges to a fracture criterion (Equation 2). The matrix response affects the transition between these two domains.

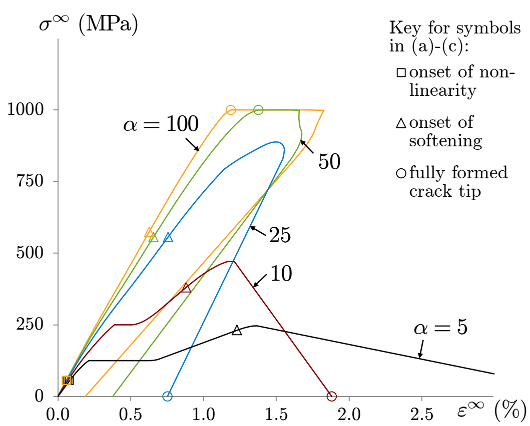

a. Overall stress–strain response of composites with a strain–hardening matrix.

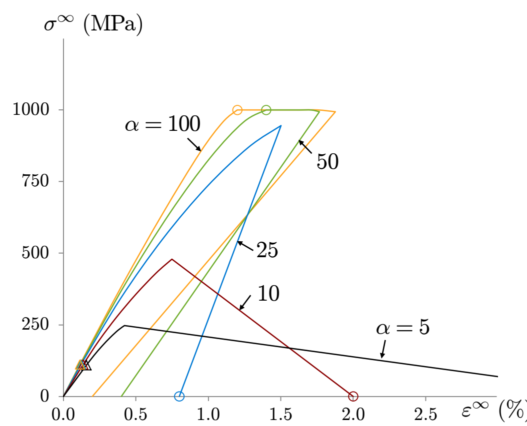

b. Overall stress–strain response of composites with a bi-linear matrix.

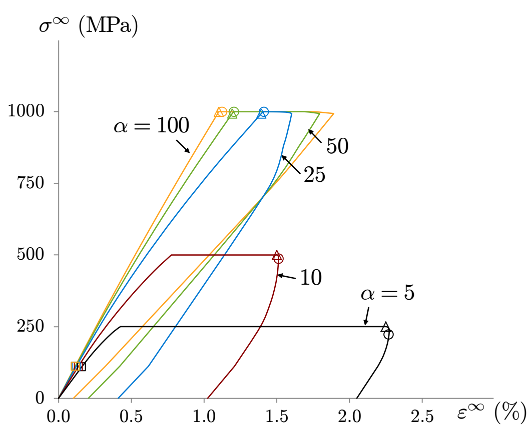

c. Overall stress–strain response of composites with a perfectly–plastic matrix.

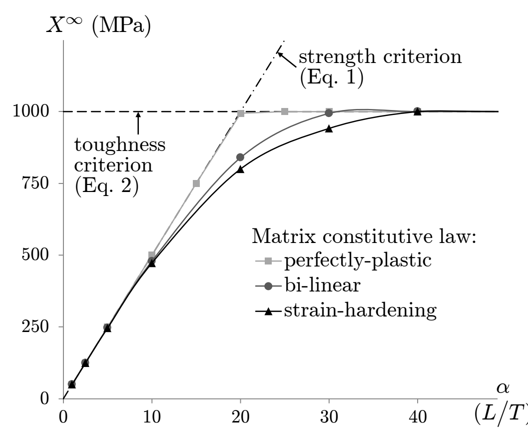

d. Effect of the characteristic aspect–ratio α on the composite's strength.

Figure 6: Effect of characteristic aspect–ratio α and matrix constitutive law on the response of composites with 'brick–and–mortar' architecture. Matrix responses are shown in Figure 5a, and all other properties are defined in Table 5.

3.3. *Effect of the thickness and volume content of the platelet and matrix phases*

The effect of varying the thickness and content of platelet and matrix phases on the response of composites is explored in Figure 7. A thicker matrix makes the composite more ductile if the platelets are thick and the matrix strain–hardens ($\alpha = 10$ in Figure 7a), but not if the platelets are slender ($\alpha = 100$ in Figure 7a) or the matrix is bi-linear (Figure 7b). The initial Young's modulus (E^{∞}) is slightly reduced by increasing the matrix thickness (Figure 7e), and the overall strength remains virtually unaffected (Figure 7f). Note that composite stresses are based on the cross section of the platelets (see Equation 7).

Using thinner platelets delays final failure and increases the strength of composites with slender configurations (see $\alpha \gtrsim 25$ in Figures 7c, 7d and 7f), and increases the ductility of composites with thicker configurations and strain–hardening matrix (see $\alpha = 10$ in Figure 7c).

3.4. *Effect of matrix toughness and geometric scaling*

Figure 8 shows that reducing the fracture toughness $\mathcal{G}^{\mathtt{m}}_{\mathrm{IIc}}$ has no influence on the loading response of composites with thick platelets (see coincident rising curves for $\alpha = 5$ in Figure 8a). However, slender configurations undergo premature crack initiation if the matrix is less tough; this can be seen in in Figures 8a–8b, by comparing the two sets of curves with distinct matrix toughnesses ($\mathcal{G}^{\mathtt{m}}_{\mathrm{IIc}} = 1.0$ kJ/m^2 and $\mathcal{G}^{\mathtt{m}}_{\mathrm{IIc}} = 0.5$ kJ/m^2) and nominal 2D geometry (with T and $t^{\mathtt{m}}$ defined in Table 5, identified by the '1:1 scale' label) when $\alpha \gtrsim 25$.

The effect of reducing $\mathcal{G}^{\mathtt{m}}_{\mathrm{IIc}}$ can be counter–balanced by proportionally scaling down the 2D geometry of the composite (i.e. by reducing T, $t^{\mathtt{m}}$ and L by the same factor). This is illustrated in Figure 8, which shows two sets of perfectly coincident stress–strain curves: the first set (labelled as '$\mathcal{G}^{\mathtt{m}}_{\mathrm{IIc}} = 1.0$ kJ/m^2, 1:1 scale') considers the nominal toughness and geometry (i.e. with T, $t^{\mathtt{m}}$ and $\mathcal{G}^{\mathtt{m}}_{\mathrm{IIc}}$ as in Table 5) and the aspect–ratios shown, while the second set (labelled as '$\mathcal{G}^{\mathtt{m}}_{\mathrm{IIc}} = 0.5$ kJ/m^2, 1:2 scale') considers halved nominal values for T, $t^{\mathtt{m}}$ and $\mathcal{G}^{\mathtt{m}}_{\mathrm{IIc}}$, and the same aspect–ratios. Figure 8 considers a strain–hardening matrix, but similar effects were observed for a wide range of different matrix constitutive laws.

4. Discussion

4.1. *Mechanical response of composites with 'brick–and–mortar' architecture*

4.1.1. *Effect of geometric configuration*

Composites with a 'brick–and–mortar' architecture can present a wide range of mechanical responses, which depend largely on the characteristic aspect–ratio $\alpha = L/T$. Assuming that the platelets withstand the applied stresses, two types of configuration were identified in Section 3:

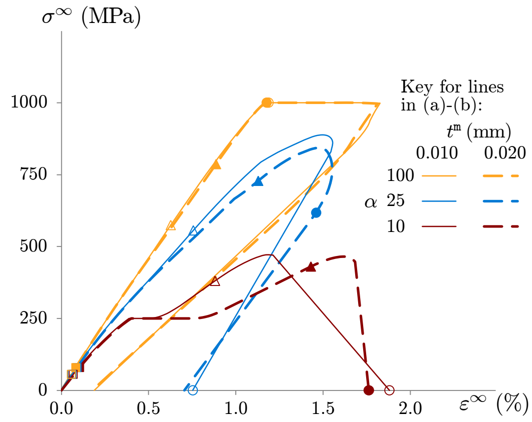

a. Response of composites with a strain–hardening matrix of different thicknesses.

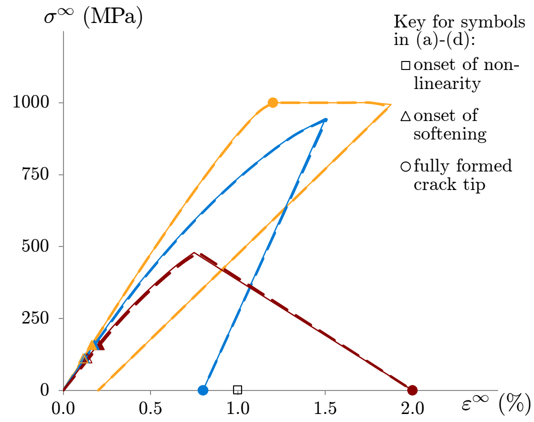

b. Response of composites with a bi-linear matrix of different thicknesses.

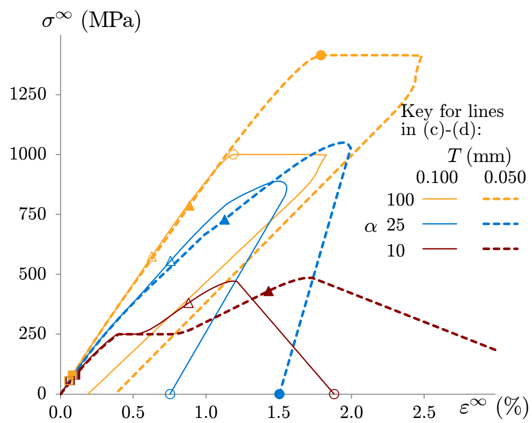

c. Response of composites with different platelet thicknesses and a strain–hardening matrix.

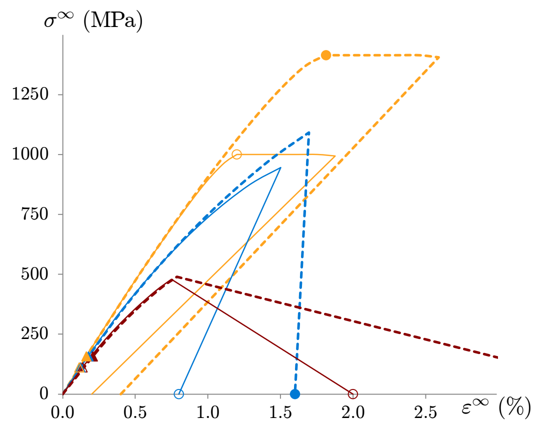

d. Response of composites with different platelet thicknesses and a bi-linear matrix.

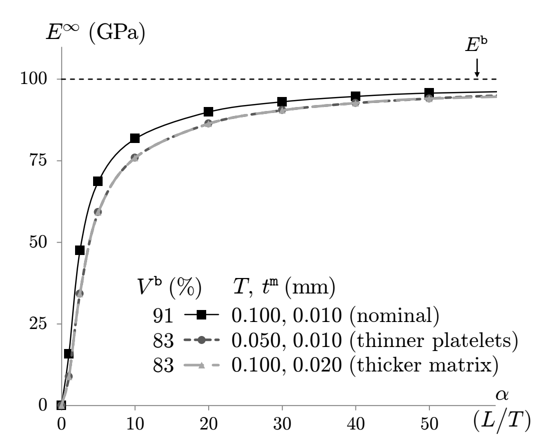

e. Initial stiffness of composites vs. characteristic aspect ratio, for different platelet and matrix thicknesses and a strain–hardening matrix.

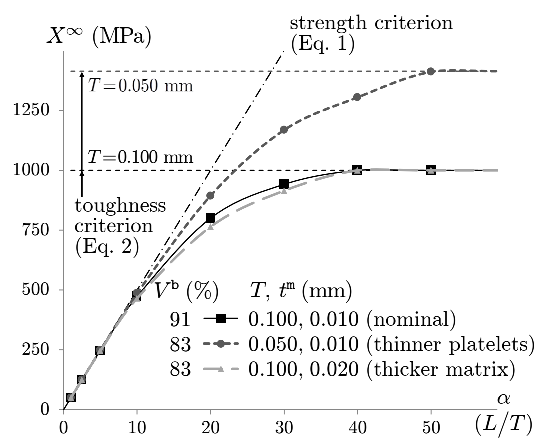

f. Strength of composites vs. characteristic aspect ratio, for different platelet and matrix thicknesses and a strain–hardening matrix.

Figure 7: Effect of the thickness and content of the platelets and matrix on the response of composites. Matrix responses are shown in Figure 5a, and other properties are defined in Table 5 unless stated otherwise. Note that composite stresses are calculated neglecting the matrix thickness (see Equation 7).

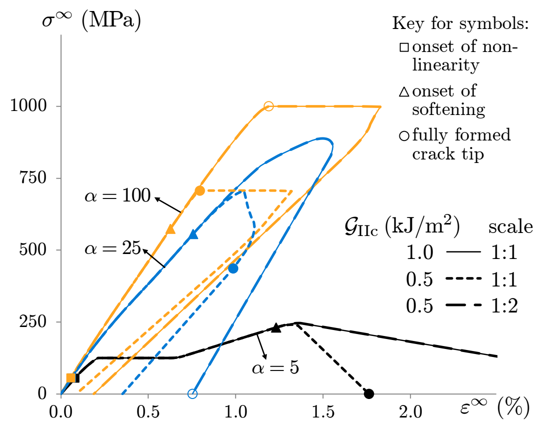

a. Overall stress–strain response of composites.

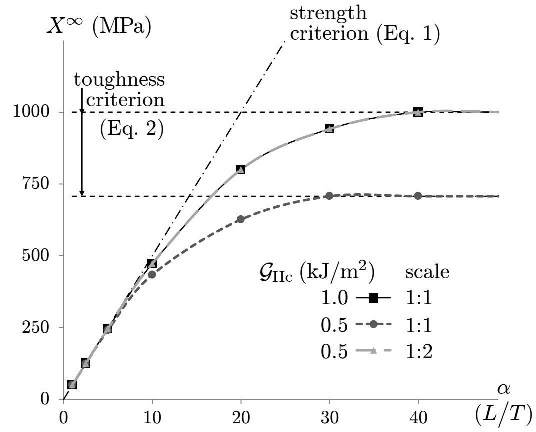

b. Composite's strength vs. platelet aspect–ratio.

Figure 8: Effect of matrix fracture toughness and geometric scaling on the response of composites with a strain–hardening matrix. Input properties are defined in Table 5 unless otherwise stated; the 1:2 scale corresponds to $T = 0.050$ mm and $t^{\mathtt{m}} = 0.005$ mm.

- *Thick geometries* (small α) are *governed by matrix plasticity* and have nearly homogeneous shear stresses along the overlapping region (Figure 5c). Consequently, the composite's stress–strain curve is similar to that of the matrix under shear (compare curves for $\alpha \lesssim 10$ in Figure 6a–6c with those in Figure 5a), and the overall strength follows a yielding criterion (Equation 1, governed by the matrix's shear strength, see Figures 6d, 7f and 8b for $\alpha \lesssim 10$);
- *Slender geometries* (large α) are *governed by matrix fracture*, following the formation of a crack tip at the platelets' ends (Figure 5e). The strength of the composite can be predicted by fracture mechanics (Equation 2, governed by the mode–II toughness of the matrix or of the matrix–platelet interface, see Figures 6d, 7f and 8b for $\alpha \gtrsim 40$), after which crack propagation occurs at constant load (see Figure 6a–6c for $\alpha \gtrsim 50$).

The transition between these cases depends on the relation between L and process zone lengths (Section 2.4). The composite is *plasticity–governed* when $L < \min\{\ell_{\mathtt{pz}}^{[i]}\}$ (stress fields are dominated by a single matrix subdomain at each instant), and *fracture–governed* when $L > \ell_{\mathtt{pz}}^{[2,\ldots,N]}$ (the entire matrix process zone fits in half of the overlapping length, and a crack tip can be formed). For a given matrix response, $\ell_{\mathtt{pz}}^{[i]} \propto \sqrt{T \cdot t^{\mathtt{m}} \cdot E^{\mathtt{b}}}$ (see Table 2), thus a plasticity–governed configuration will transition to fracture–governed by increasing the ratio $L/\ell_{\mathtt{pz}}^{[i]}$, hence by increasing the factor $\sqrt{(\alpha/E^{\mathtt{b}}) \cdot (L/t^{\mathtt{m}})}$.

4.1.2. Non-linear response and matrix effects

Composites with a 'brick–and–mortar' architecture can show a non-linear response with progressive failure due to matrix (or interfacial) shearing, by one of the following mechanisms:

(i) *Non-linear matrix response*, effective in *thick configurations* when the matrix presents significant plasticity and strain hardening before softening (see $\alpha \lesssim 10$ in Figures 6a and 6c). The composite becomes more ductile if the matrix content increases (i.e. when $t^{\mathtt{m}}$ increases or T decreases, see Figures 7a and 7c), or if the matrix's failure strain increases (as the composite's stress–strain curve reproduces that of the matrix for small α, compare Figures 7a–7c with Figure 5a);

(ii) *Progressive crack formation in the matrix* (or matrix–platelet interface), which occurs in *slender configurations* with $L \approx \ell_{\mathtt{pz}}^{[2,\dots,N]}$ (see $\alpha = \{25, 50\}$ in Figures 5–6). In this case, a damage process zone develops along a great part of the overlapping length, resulting in progressive loss of stiffness due to matrix softening. This mechanism is enhanced by thinner platelets or a tougher matrix (see $\alpha \gtrsim 25$ in Figures 7c–7d and 8a), and it is mostly independent of the matrix thickness and constitutive law (see Figures 7a–7b).

4.1.3. Macroscopic response

Figures 5 to 8 show the response of a single composite unit–cell, as seen in Figure 1b. To understand the macroscopic response of the composite, consider now a chain of n identical unit–cells in series. Along the loading phase (with positive tangent stiffness), $\sigma_{\mathtt{M}}^{\infty} \equiv \sigma_{\mathtt{uc}}^{\infty}$ and $\varepsilon_{\mathtt{M}}^{\infty} \equiv \varepsilon_{\mathtt{uc}}^{\infty}$ (where `M` and `uc` represent respectively the macroscopic and unit–cell responses). However, due to intrinsic material variability, one weaker cell will reach its strength X^{∞} (and associated failure strain e^{∞}) first, after which deformation will localise. Consequently, the weakest cell will follow its equilibrium softening response, while the remaining cells will unload elastically (subscript `un` in Equation 12a), leading to the macroscopic unloading response calculated in Equation 12b:

$$\begin{cases} \sigma_{\mathtt{un}}^{\infty} \equiv \sigma_{\mathtt{uc}}^{\infty} \\ \varepsilon_{\mathtt{un}}^{\infty} = e_{\mathtt{uc}}^{\infty} - \left(X^{\infty} - \sigma_{\mathtt{un}}^{\infty}\right)/E^{\infty} \end{cases}, \tag{12a}$$

$$\begin{cases} \sigma_{\mathtt{M}}^{\infty} \equiv \sigma_{\mathtt{uc}}^{\infty} \\ \varepsilon_{\mathtt{M}}^{\infty} = \left[\varepsilon_{\mathtt{uc}}^{\infty} + (n-1)\cdot\varepsilon_{\mathtt{un}}^{\infty}\right]/n \end{cases}. \tag{12b}$$

Figure 9 compares the response of a unit–cell ($n = 1$) to that of a finite composite volume (finite n) or of an infinitely large ($n \to \infty$) sample. This shows that:

a. All non-linearities developed in the unit–cell before the strength is reached are reproduced in the macroscopic response. Thick configurations with a strain–hardening matrix dissipate a significant amount of energy through diffuse plasticity and damage (Figure 9a);

b. Stress plateaus at $\sigma^{\infty} \approx X^{\infty}$ are not replicated in the macroscopic response, as softening starts just below the plateau level of the n–1 infinitesimally stronger cells; permanent strains and energy dissipation through plasticity or damage are therefore negligible (Figure 9b).

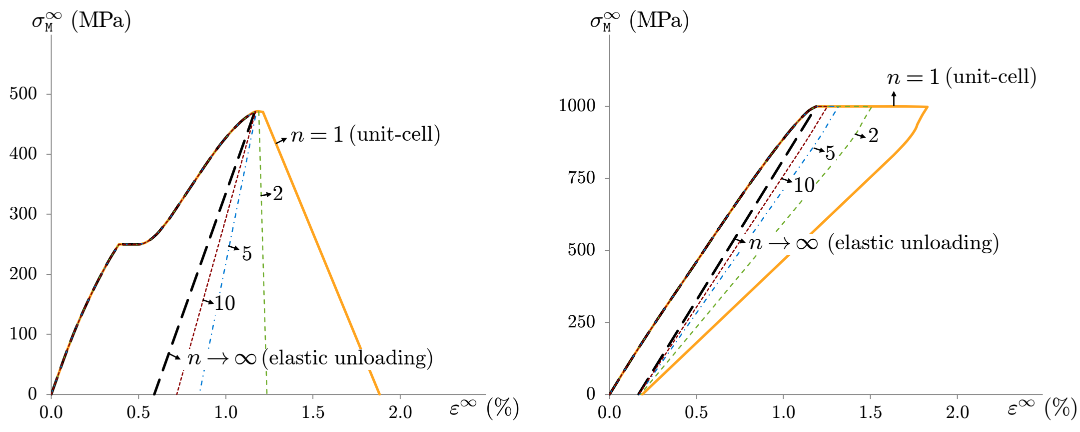

a. Unit–cell with strain–hardening ($\alpha = 10$).

b. Unit–cell with stress plateau ($\alpha = 100$).

Figure 9: Macroscopic stress–strain response of composites with 'brick–and–mortar' architecture with n unit–cells in series. Both cases consider the nominal geometry and properties (Table 5), and a strain–hardening matrix.

c. The unloading response is governed by the overall size of a structure [14]. Even a material with stable progressive failure at the small scale will fail unstably if loaded in a sufficiently large structure (compare $n = 1$ with $n \to \infty$ in Figure 9a).

4.2. Optimal configuration for brittle matrix systems

Figure 9b shows that, as soon as a crack tip forms in the matrix, it propagates at constant load leading to damage localisation — which limits ductility and energy absorption. Consequently, *progressive crack formation in the matrix* (see Section 4.1.2) generates macroscopic non-linearities only before a crack tip is formed (i.e. before reaching the stress plateau).

Because this mechanism operates in toughness–governed configurations (see Figure 6d), in order to fully utilise the tensile strength of the platelets one must impose that:

$$X_{\mathcal{G}}^{\infty} = X^{\mathtt{b}}/2 \quad \text{(where } X_{\mathcal{G}}^{\infty} \text{ is given from Eq. 2), hence} \qquad T^{\star} = 4 \cdot E^{\mathtt{b}} \cdot \mathcal{G}_{\mathrm{IIc}}^{\mathtt{m}} / (X^{\mathtt{b}})^2 \, . \tag{13}$$

This defines the optimal characteristic thickness: if $T < T^{\star}$ the platelets fail under tension before the matrix fractures, and vice–versa (see Figure 10a).

The effect of progressive matrix fracture is fairly independent of the matrix thickness and constitutive law (see Figures 7a–7b), hence a thin bi-linear matrix ($N = 2$) is considered for simplicity. According to Figure 6b and Section 4.1.1, a crack tip can fully form in configurations with $L \geq \ell_{\mathtt{pz}}^{[2,\ldots,N]}$, but the non-linearity before the stress plateau decreases as L increases further. The optimal characteristic length is therefore defined in this case as:

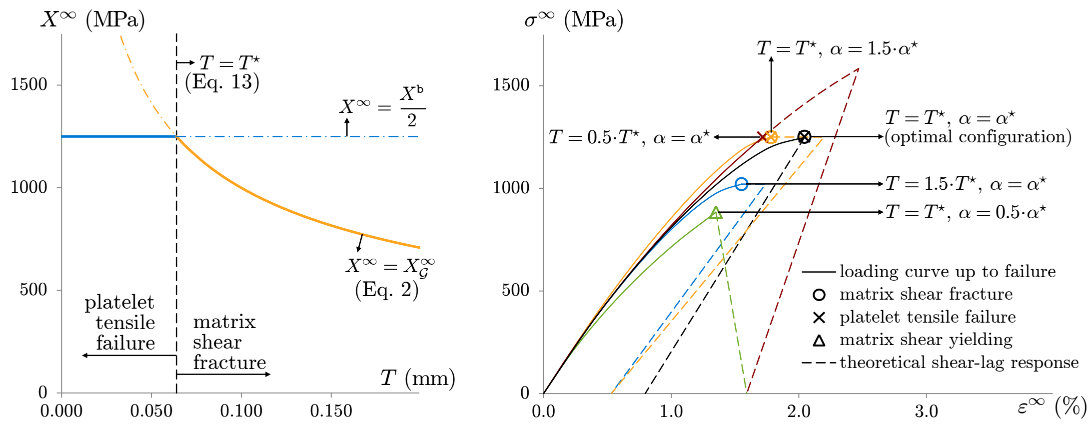

a. Strength of slender configurations and definition of the optimal thickness $T^\star$.

b. Response of the optimised configuration for matrix fracture (see Equations 13 and 14c) and its variations.

Figure 10: Response of composites with 'brick–and–mortar' architecture with slender configurations and a bi-linear matrix response. For the nominal properties in Table 5, $T^\star\!=\!0.064$ mm, $L^\star\!=\!2.513$ mm and $\alpha^\star\!=\!39.3$).

$$L^\star = \ell_{\mathtt{pz}}^{[N\equiv 2]}\,, \quad \text{which following Eq.(h) in Table 2 leads to} \quad L^\star = \frac{\pi}{2}\cdot\sqrt{\frac{T\cdot t^{\mathtt{m}}\cdot E^{\mathtt{b}}}{2\cdot|G^{[N\equiv 2]}|}}\,. \tag{14a}$$

For a thin, brittle bi-linear matrix phase with maximum shear strength $S^{\mathtt{m}}$,

$$\gamma^{[N]} \overset{(\text{Eq.8})}{=} \frac{2\cdot\mathcal{G}^{\mathtt{m}}_{\mathrm{IIc}}}{S^{\mathtt{m}}\cdot t^{\mathtt{m}}} \quad \text{and} \quad \gamma^{[N]}-\gamma^{[1]}\approx\gamma^{[N]}\,, \quad \text{hence} \quad G^{[N]} = \frac{S^{\mathtt{m}}}{\gamma^{[N]}-\gamma^{[1]}} \approx \frac{(S^{\mathtt{m}})^2\cdot t^{\mathtt{m}}}{2\cdot\mathcal{G}^{\mathtt{m}}_{\mathrm{IIc}}}\,; \tag{14b}$$

replacing in Equation 14a,

$$L^\star \approx \frac{\pi}{2\cdot S^{\mathtt{m}}}\cdot\sqrt{2\cdot T\cdot E^{\mathtt{b}}\cdot\mathcal{G}^{\mathtt{m}}_{\mathrm{IIc}}}\,. \tag{14c}$$

A composite with optimal dimensions $T^\star$ and $L^\star$ will therefore fail at:

$$\sigma^\infty = X^\infty_{\mathcal{G}} = \frac{X^{\mathtt{b}}}{2} \quad \text{and} \quad \varepsilon^\infty = e^\infty = \frac{t^{\mathtt{m}}\cdot\gamma^{[N]}}{2\cdot L^\star} + \frac{X^{\mathtt{b}}}{2\cdot E^{\mathtt{b}}} \qquad \text{(following Equation 7).} \tag{15a}$$

Replacing $\gamma^{[N]}$ and $L^\star$ according to Equations 14b–14c, and then defining $T\!=\!T^\star$ from Equation 13 yields:

$$e^\infty = \frac{2}{\pi}\cdot\sqrt{\frac{\mathcal{G}^{\mathtt{m}}_{\mathrm{IIc}}}{T\cdot E^{\mathtt{b}}}} + \frac{X^{\mathtt{b}}}{2\cdot E^{\mathtt{b}}} \implies e^\infty = \left(\frac{1}{\pi}+\frac{1}{2}\right)\cdot\frac{X^{\mathtt{b}}}{E^{\mathtt{b}}}. \tag{15b}$$

Figure 10b presents the response of a composite with 'brick–and–mortar' geometry optimised for matrix fracture (defined by $T^\star$ and $\alpha^\star = L^\star/T^\star$, following Equations 13 and 14c).

While this mechanism leads to non-linearity and progressive failure, it has limited potential for ductility (as the optimal configuration with thin bi-linear matrix will fail at a strain $e^{\infty} \approx 82\% \cdot e^{\mathsf{b}}$, where e^{b} is the failure strain of the linear–elastic platelets, see Equation 15b). Modifying the optimal geometry results in further loss of strength and/or failure strain.

4.3. Analysis of the proposed model in the scope of the literature

The analytical model for composites with 'brick–and–mortar' architecture presented in this paper complements existing literature with the following features:

a. This model bridges the two most widely used theories for sub-critical discontinuous composites: (i) yield–slip theory (governed by the shear strength of the matrix) [5] and (ii) fracture mechanics (governed by the mode–II toughness of the matrix or interface) [6, 7]. While there is significant debate in the literature [8–13] on which criterion should be used for different types of matrix, Figure 6d shows that they are both accurate for most matrices, but limited in the range of applicable geometries of the platelets or inclusions;

b. The model predicts non-linear size effects on the strength of composites with 'brick–and–mortar' architecture, tending to plasticity theory for thick (small α) platelets, and to fracture mechanics for slender (large α) platelets. The characteristic length of the damage process zone (calculated in Equation 10 and Table 2) defines the transition between the two asymptotic responses, which agrees with Bazant's size–effect law [14];

c. This is the first analytical model in the literature to consider a generic non-linear response (as long as it is piecewise linear) for the soft phase, thus providing a flexible tool for investigating the effect of different matrices on the response of discontinuous composites;

d. Due to its analytical formulation, this model calculates the full response and local fields in less than 1 second, while considering a completely non-linear matrix response. The model is thus particularly suitable for parametric studies and Monte-Carlo analyses.

e. The model can be extended to staggered discontinuous composites with other types of inclusions (by having $T = A^{\mathsf{b}}/C^{\mathsf{b}}$, where A^{b} is the area and C^{b} is the perimeter of the inclusions' cross–section), or to composites with randomly shifted platelet–ends, platelets with stochastic strength or complex load sharing laws [16, 17]. These developments will be the scope of further publications.

5. Conclusions

An analytical model for the tensile response of perfectly staggered discontinuous composites was developed. The model is based on shear–lag, and considers a generic piecewise linear matrix constitutive law (including non-linearity and fracture). Process zone lengths are calculated and used in an efficient implementation framework, thus the full equilibrium response of composites with 'brick–and–mortar' architecture is determined almost instantaneously.

Parametric studies showed that the response of composites with thick platelets are dominated by plasticity, while those with slender platelets are governed by fracture mechanics. This leads to non-linear size effects influenced by the length of the matrix's damage process zone.

Results suggest that well-designed discontinuous composites can present progressive failure, energy dissipation and enhanced failure strains, achieved by two different mechanisms: plasticity and strain–hardening of the matrix (leading to ductile composites with modest strength), and fracture of the matrix (leading to strong composites with non-linear response). This concept is experimentally demonstrated in a subsequent paper [18].

Acknowledgements

This work was funded under the EPSRC Programme Grant EP/I02946X/1 on High Performance Ductile Composite Technology, in collaboration with the University of Bristol.

Appendix A. Finite Element validation of the proposed analytical model

The analytical model was validated by 2D FE analyses illustrated in Figure A.1, with nominal dimensions and properties defined in Table 5. The platelets were modelled as an isotropic linear–elastic material with Young's modulus $E^{\mathtt{b}}$ and Poisson's ratio $\nu^{\mathtt{f}} = 0.3$. The matrix was modelled as an isotropic material with initial linear–elastic behaviour (with Young's modulus $E^{\mathtt{m}} = 2 \cdot G^{\mathtt{m}} \cdot (1 + \nu^{\mathtt{m}})$ and matrix Poisson's ratio $\nu^{\mathtt{m}} = 0.5$); its non-linear response was modelled by von Mises plasticity, where the von Mises equivalent stresses ($\sigma_{\mathrm{vM}}^{[i]}$) and strains ($\varepsilon_{\mathrm{vM}}^{[i]}$) were calculated from the stress–strain curve of a strain–hardening matrix under shear (see Figure 5a) as:

$$\sigma_{\mathrm{vM}}^{[i]} = \sqrt{3} \cdot \tau^{[\mathrm{i}]} \qquad \text{and} \qquad \varepsilon_{\mathrm{vM}}^{[i]} = \frac{\sqrt{3}}{3} \cdot \gamma^{[\mathrm{i}]} \,. \tag{A.1}$$

Two characteristic lengths ($L = 1.0$ mm and $L = 5.0$ mm) were considered. The models were discretised using 4–nodes elements with full integration; one element was used to represent the matrix's through–the–thickness direction, and five elements for the platelets. The models were run under displacement control using Abaqus Standard [19] implicit solver, assuming plane stress, plane strain or generalised plane strain.

The deformed shape of the composite unit–cell with thick platelets is represented in Figure A.1a, where the fields represent the longitudinal stresses in the platelets and shear stresses in the matrix. It is confirmed that platelet stresses are generally uniform across their thickness, with the largest through–the–thickness variation found near the end of platelet $\mathcal{A}$. This

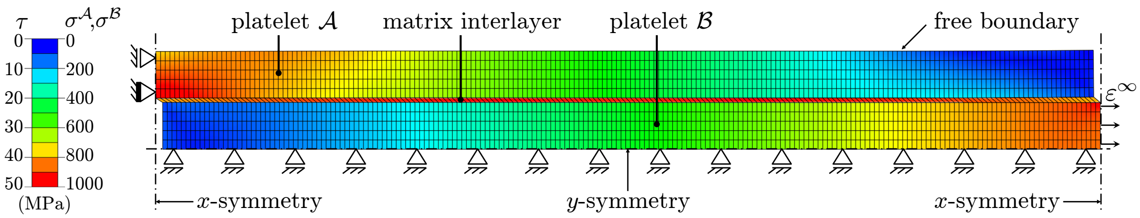

a. Overview of the FE geometry, mesh and boundary conditions. The fields ($\sigma^{\mathcal{A}}$ and $\sigma^{\mathcal{B}}$ in the platelets, and τ in the matrix) are shown on the deformed shape at the maximum load for $L=1$ (plane stress model).

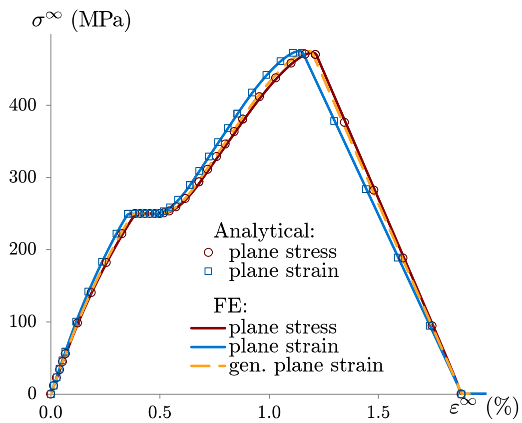

b. FE vs. analytical global stress–strain responses for L = 1 mm, considering different 2D states.

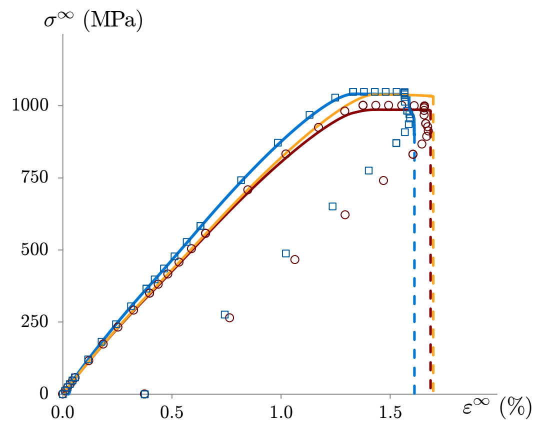

c. FE vs. analytical global stress–strain responses for L = 5 mm, considering different 2D states.

Figure A.1: Finite Element model and results for the composite unit–cell (represented in Figure 1b), considering a strain–hardening matrix.

variation is due to bending of platelet $\mathcal{A}$, induced by its free upper boundary; it was verified that the resulting mode–I component of the energy release rate at the matrix interlayer was approximately half of the mode–II component.

Figure A.1b shows a remarkable agreement between analytical and FE models for composites with short platelets, both for plane stress and plane strain conditions (as long as the corresponding platelet stiffness E^{b} takes the 2D state into account). Similar agreement was found for the configuration with slender platelets (in Figure A.1c), although the analytical equilibrium unloading path could not be captured by the FE model under remote displacement control.

References

[1] F. Barthelat and R. Rabiei. Toughness amplification in natural composites. *Journal of the Mechanics and Physics of Solids*, 59(4):829–840, 2011.

[2] M. A. Meyers, P.-Y. Chen, A. Y.-M. Lin, and Y. Seki. Biological materials: Structure and mechanical properties. *Progress in Materials Science*, 53(1):1–206, 2008.

[3] F. Barthelat, A. K. Dastjerdi, and R. Rabiei. An improved failure criterion for biological and engineered staggered composites. *Journal of the Royal Society Interface*, 10(79), 2013.

[4] M. R. Begley, N. R. Philips, B. G. Compton, D. V. Wilbrink, R. O. Ritchie, and M. Utz. Micromechanical models to guide the development of synthetic 'brick and mortar' composites. *Journal of the Mechanics and Physics of Solids*, 60(8):1545–1560, 2012.

[5] A. Kelly and W. R. Tyson. Tensile properties of fibre–reinforced metals: Copper/tungsten and copper/molybdenum. *Journal of the Mechanics and Physics of Solids*, 13(6):329–338, 1965.

[6] J. O. Outwater and M. C. Murphy. Fracture energy of unidirectional laminates. *Modern Plastics*, 47(September issue):160–168, 1970.

[7] Y.-C. Gao, Y.-W. Mai, and B. Cotterell. Fracture of fiber–reinforced materials. *Journal of Applied Mathematics and Physics*, 39(4):550–572, 1988.

[8] H. Stang, Z. Li, and S. P. Shah. Pullout problem — stress versus fracture mechanical approach. *Journal of Engineering Mechanics*, 116(10):2136–2150, 1990.

[9] C. K. Y. Leung. Fracture–based two–way debonding model for discontinuous fibres in elastic matrix. *Journal of Engineering Mechanics*, 118(11):2298–2318, 1992.

[10] M. R. Piggott, M. Ko, and H. Y. Chuang. Aligned short-fibre-reinforced thermosets — experiments and analysis lend little support for established theory. *Composites Science and Technology*, 48(1-4):291–299, 1993.

[11] J. A. Nairn. On the use of shear–lag methods for analysis of stress transfer in unidirectional composites. *Mechanics of Materials*, 26(2):63–80, 1997.

[12] S. Zhandarov, E. Pisanova, and B. Lauke. Is there any contradiction between the stress and energy failure criteria in micromechanical tests? Part I. Crack initiation: stress–controlled or energy–controlled? *Composite Interfaces*, 5(5):387–404, 1998.

[13] P. Zinck, H. D. Wagner, L. Salmon, and J. F. Gerard. Are microcomposites realistic models of the fibre/matrix interface? I. Micromechanical modelling. *Polymer*, 42(12):5401–5413, 2001.

[14] Z. P. Bažant. Size effect on structural strength: a review. *Archive of Applied Mechanics*, 69(9-10):703–725, 1999.

[15] H. D. Espinosa, A. L. Juster, F. J. Latourte, O. Y. Loh, D. Gregoire, and P. D. Zavattieri. Tablet–level origin of toughening in abalone shells and translation to synthetic composite materials. *Nature Communications*, 2:173, 2011.

[16] H. F. Lei, Z. Q. Zhang, and B. Liu. Effect of fiber arrangement on mechanical properties of short fiber reinforced composites. *Composites Science and Technology*, 72(4):506–514, 2012.

[17] M. Nishikawa, T. Okabe, and N. Takeda. Periodic-cell simulations for the microscopic damage and strength properties of discontinuous carbon fiber-reinforced plastic composites. *Advanced Composite Materials*, 18(1):77–93, 2009.

[18] G. Czél, S. Pimenta, M. R. Wisnom, and P. Robinson. Demonstration of pseudo–ductility in unidirectional discontinuous carbon fibre / epoxy prepreg composites. *Composites Science and Technology*, (submitted) 2014.

[19] Dassault Systemes Simulia Corp. Abaqus 6.11 Analysis User's Manual, 2011.